Front. Mater. Sci. 2024, 18(4): 240709
https://doi.org/10.1007/s11706-024-0709-5

REVIEW ARTICLE

Application of SEM-CL system in the characterization of material microstructures

Rongrong Jiang, Yirong Yao, Jianmin Guan, Jiafeng Shen, Huanming Lu (✉), and Ming Li (✉)

Test Center, Ningbo Institute of Materials Technology and Engineering, Chinese Academy of Sciences, Ningbo 315201, China

ABSTRACT: Cathodoluminescence (CL) characterization technology refers to a technical approach for evaluating the luminescent properties of samples by collecting photon signals generated under electron beam excitation. By detecting the intensity and wavelength of the emitted light, the energy band structure and forbidden bandwidth of a sample can be identified. After a CL spectrometer is mounted on a scanning electron microscope (SEM), functions are integrated, such as high spatial resolution, morphological observation, and energy-dispersive spectroscopy (EDS) to analyze samples, offering unique and irreplaceable advantages for the microstructural analysis of certain materials. This paper reviews the applications of SEM-CL systems in the characterization of material microstructures in recent years, illustrating the utility of the SEM-CL system in various materials including geological minerals, perovskite materials, semiconductor materials, non-metallic inclusions, and functional ceramics through typical case studies.

KEYWORDS: scanning electron microscope; cathodoluminescence; geological mineral; perovskite material; semiconductor material; non-metallic inclusion; functional ceramic

Contents

Received September 3, 2024; accepted November 5, 2024

E-mails: liming@nimte.ac.cn (M.L.), hmlu@nimte.ac.cn (H.L.)

1 Introduction

Certain atoms, when subjected to external energy stimulation, experience transitions of some electrons

surrounding the nucleus from their original orbits to those of higher energy levels, namely, from the ground state to the excited state. Given that the excited state is inherently unstable, it tends to revert to the ground state. During this transition, the excess energy is released in the form of light, resulting in luminescence [1–3]. The luminescence signal is closely associated with the atomic species, valence state, and band gap characteristics. Consequently, the analysis of luminescence spectra can yield a wealth of information regarding the photoelectric properties of materials, energy band structures, band gap widths, chemical compositions, impurities, structural defects, phase compositions, and so on.

The excitation sources for inducing luminescence include light and electrons, leading to the development of analytical methods such as photoluminescence (PL) and electroluminescence (EL). For PL, light sources like mercury lamps and lasers are used, with the light spot typically at the millimeter scale. EL, on the other hand, involves the application of voltage to the material to generate luminescence spectra. Regardless of whether it is PL or EL, their imaging capabilities are inadequate to meet the requirements for visualized micro-regional analysis. Furthermore, the sample preparation for EL is notably complex. Among various visualization analysis tools, scanning electron microscope (SEM) is a highly advantageous instrument, offering simple sample preparation, large depth of field, and high resolution. The luminescence signals generated by the excitation of sample micro-regions with an electron beam are referred to as cathodoluminescence (CL), a term derived from the initial designation of the electron beam as cathode rays [1–4]. The SEM-CL system, which integrates a SEM with a luminescence spectrometer, excels in pinpointing micro-regions for the analysis of their luminescence characteristics. Furthermore, since SEM can be equipped with a variety of functional attachments such as backscattered electron (BSE) detectors, energy-dispersive spectroscopy (EDS) detectors, electron backscatter diffraction (EBSD) systems, and high/low-temperature stages, the simultaneous application of CL technology alongside these attachments allows for a comprehensive analysis of multiple characteristics within the same micro-region of a sample, including morphologies, composition contrast, element distributions, crystallographic features, and luminescent properties, thereby yielding a more enriched dataset.

In recent years, there are a number of review articles on CL that have been published. However, these publications are predominantly material-centric, focusing on the application of CL within specific material domains such as geology [5] and perovskite materials [6]. Typically, the audience for such literature is restricted to researchers within those particular material fields. Generally, the application of CL technology is considered common knowledge by researchers in the area of luminescent materials. Yet, for materials that do not inherently luminesce, or for researchers who have had no exposure to or understanding of CL technology, there are limited opportunities to become acquainted with this technique, let alone incorporate it into their research.

This paper approaches the subject from the perspective of instrumental equipment, covering a variety of applications across different material domains. In comparison, the number of researchers conversant with SEM significantly exceeds that of researchers with a certain level of understanding of CL. Should readers become aware, through this article, that SEM can be equipped with CL capabilities, or if the analytical methods cited in the literature inspire them to consider research methodologies that transcend the inherent material properties by focusing on additional factors such as defects, impurities, and irradiation, this contrarian thinking may offer a novel perspective for materials research. Through this approach, researchers may uncover new applications of the combined SEM and CL technology within their respective fields.

This paper delineates the principles, structure, and acquisition modes of SEM-CL and summarizes the applications of SEM-CL in the microstructural characterization of various material domains, including geomineralogy [7–13], halide perovskites [6,14–18], semiconductors [19–35], non-metallic inclusions [36–40], and functional ceramics [41–46]. It is hoped that the introduction and compilation of applications of this technology provided herein will assist a broad spectrum of materials researchers in bringing a more innovative and distinctive perspective to sample analysis and characterization.

2 Principles, structure, and acquisition modes of SEM-CL

2.1 The principles of the SEM-CL system

CL was first observed in the mid-19th century as the light

emission produced when cathode ray electrons struck the glass of vacuum discharge tubes [1–2]. It is well known that when the incident electron beam in a SEM interacts with the sample, a variety of signals are produced, such as secondary electrons (SEs), BSEs, and characteristic X-rays, which serve as sources for morphological imaging, compositional contrast, and elemental analysis. In addition to these, there is another form of electromagnetic radiation, the CL signal, which, although less well known than the aforementioned signals, is equally valuable and provides unique complementary information in various material analysis techniques. It can capture energy ranges from 0.5 to 6 eV, not only offering insights into the composition, crystalline, and band gap structures of the sample, but also analyzing the impact of certain trace elements or dopants based on different optical transitions.

CL emission includes incoherent and coherent luminescence, with a schematic illustration of their principles shown in Fig. 1 [1]. When incident electrons interact with the material, a red pear-shaped interaction region as depicted forms, and the material's valence electrons are elevated to an excited state. Due to the instability of the excited state, photons are generated followed by emittance during the radiative decay process. In semiconductors and dielectrics, the excited electrons can decay directly to the valence band (band-edge emission) after entering the conduction band or through intermediate states within the band gap. In quantum-confined structures such as quantum dots, the energy bands themselves are quantized, and luminescence also occurs in the form of CL. Incoherent CL emission does not have a fixed phase relationship with the excited electrons. The diffusion of carriers can increase the volume of interaction. The resulting luminescence includes band-edge emission, intrinsic defect emission, and non-intrinsic defect emission induced by doping. Coherent luminescence refers to the situation that changes in the electron's trajectory within the dielectric environment lead to variations in the electric and magnetic fields, which can polarize the material, thereby resulting in direct radiation or surface plasmon excitation. The emitted photons in this case have a fixed phase relationship with the incident electrons.

2.2 The structure of the SEM-CL system

The CL detector probe is installed directly beneath the SEM pole piece and consists of an aluminum-coated parabolic reflector with a small central aperture that allows the electron beam to pass through and strike the sample, thereby exciting the surface of the sample to generate fluorescence signals. A schematic diagram of its operating principle is shown in Fig. 2(a) [6,47]. Light signals are reflected by the parabolic mirror to form the parallel light that enters the spectrometry system. A knob at the entrance of the spectrometry system can switch between two different operating modes: panchromatic mode (also known as full-light mode) and monochromatic mode (also known as single-light mode). In panchromatic mode, the light passes through several reflective mirrors and directly reaches the signal detector. In monochromatic mode, the light signals pass through a slit into the spectrometry system. Utilizing the property that light of different wavelengths has different refractive angles, and the diffraction grating decomposes the mixed light into light of different wavelengths. After filteration by the grating, light of specific wavelengths then reaches the signal detector.

2.3 Acquisition modes of the SEM-CL system

Different SEM-CL systems are equipped with various

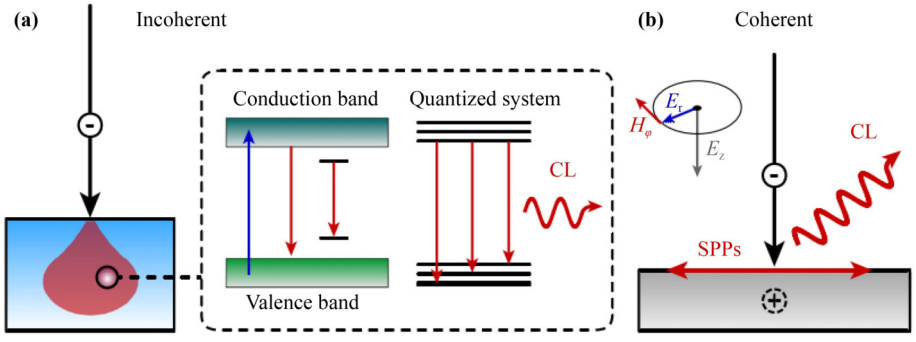

Fig. 1 (**a**) Schematic representation of incoherent CL generation. (**b**) For coherent excitation. Reproduced with permission from Ref. [1].

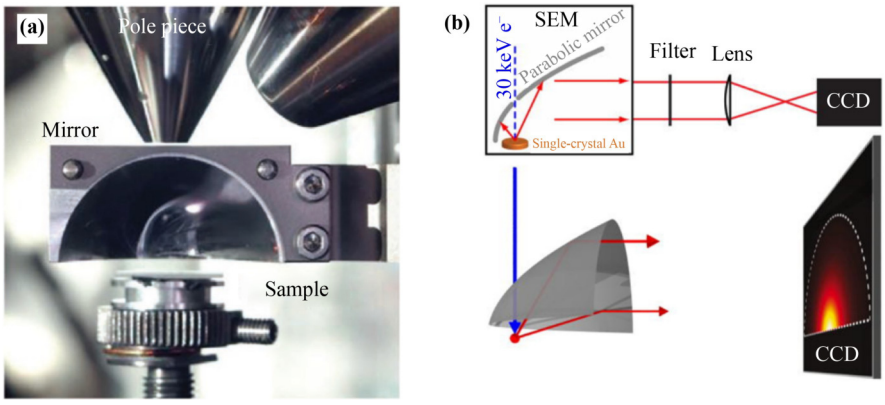

Fig. 2 (**a**) Photograph of a light collection system in an SEM chamber. (**b**) Schematic overview of the angular resolution experimental setup. Reproduced with permission from Refs. [6,47].

acquisition modes. The most comprehensive acquisition modes currently available include the following:

1) Imaging mode: This mode includes panchromatic imaging and monochromatic imaging. In panchromatic imaging, the wavelength is unfiltered, and the acquisition captures the overall luminescence image within the micro-region, with the image contrast corresponding to the total luminescence intensity across all wavelengths. In monochromatic imaging, the wavelength is filtered. The acquisition is limited to the luminescence image that has been filtered for a particular wavelength, with the image contrast representing the luminescence intensity of that specific wavelength.

2) Spectroscopy mode: This mode collects wavelength-resolved luminescence spectra from a single point or region. The spectrum plot has wavelength or energy on the horizontal axis and counts on the vertical axis, corresponding to luminescence intensity.

3) Spectral imaging mode: This mode enables the acquisition of wavelength-resolved spectra at each step size during line scanning or area scanning. Then, such spectra are converted into points with distinct contrast to delineate corresponding lines or images that represent the luminescence characteristics. Additionally, the gray contrast can be rendered into false-color RGB, which provides a more intuitive representation of the luminescence. Of course, you can also select any point in the scan results to view its emission spectrum.

4) Angular resolution mode: This mode enables the acquisition of angularly resolved luminescence characteristic images. Since the CL signal is collected by a parabolic reflector, it can be inferred from the geometric positional relationship that each specific location on the detector corresponds to a particular emission angle [47–48]. By back-projecting the acquired two-dimensional (2D) luminescence information, the angular space corresponding to the sample's respective positions can be determined. A schematic diagram of the principle is shown in Fig. 2(b) [47]. The electron beam passes through a hole in the reflector to reach the sample. The resulting CL signal is then projected onto a charge-coupled device (CCD) camera, and the parabolic beam is projected onto an isotropic light source CCD array, thereby determining the three-dimensional (3D) angular distribution of the CL emission.

5) Simultaneous wavelength and angle resolution mode: This mode utilizes a specialized rectangular aperture to collect the signal at specific emission angles followed by spectroscopic analysis for the purpose of obtaining the wavelength distribution over a defined angular range. This process ultimately yields comprehensive information on the emission angles and wavelengths across the entire range of luminescence angles.

3 Applications of SEM-CL in the field of geomineralogy research

CL has a long history of application in the field of geological mineralogy and has been used in research since the mid-20th century. This type of CL system uses a non-focused cold cathode or hot cathode to excite the sample to observe the CL color. It is primarily utilized for the identification and classification of minerals that cannot be distinguished morphologically via optical microscopy (OM) [49–53]. For instance, Weiss et al. [53] employed a traditional CL system in conjunction with OM to classify pottery from the Yeha region, thereby supporting local

archaeological research. Figure 3 illustrates the CL imaging of six pottery fragments classified by color, allowing for a more refined classification based on CL color. Götte et al. [49] conducted a detailed CL study of the mineral quartz, observing the CL color change from initial to final state under increasing irradiation. The variation in CL color is dependent on the defect structure of quartz grains, which is determined by the physicochemical conditions during the crystallization process. Consequently, CL color changes can be used to aid in tracing the origin of quartz grains, as demonstrated in Fig. 4 [49].

Conventional CL allows for the observation of a large area, as indicated by the scale bars in Figs. 3 and 4, with the observation regions being on the millimeter scale, due to the large diameter of the beam spot size of the unfocused electron beam. However, the limitations of monolithic imaging functionality and low spatial resolution also restrict further analysis of fine structures. The integration of CL with SEM excited by focused ultra-fine electron beam significantly enhances the spatial resolution, greatly improving the investigation of more microscopic areas [7–13].

The research by Hamers et al. [8] not only exploits the high-resolution capabilities of the SEM-CL technology, but also employs the aforementioned SEM accessories such as BSE, EDS, and EBSD to investigate changes in the microstructure of quartz during the low-velocity shear deformation. This includes the examination of cracks, grain slip, grain size, and grain orientation. By studying the mechanisms by which deformation conditions affect these microstructural changes, their work offers a new perspective on the formation process of quartz. The authors present a wealth of false-color RGB-CL images superimposed with BSE images, which allows for the correlation of information such as cracks, metal element enrichments, and grain boundary channel contrast from the BSE images with the luminescent characteristics of the region. As shown in Figs. 5(a) and 5(b), luminescence in the form of blue light is emitted at grain boundaries, while the interior of the grains emits an orange-yellow light. Even when backscattered contrast indicates that it is the same grain, the luminescent color within its interior is not entirely consistent. Additionally, the application of EBSD further analyzes the range of grain boundary angles and crystal orientation densities during the deformation of quartz, as shown in Fig. 5(c). The pole figure (Figs. 5(d) and 5(e)) visually represents no significant difference between the texture of the refined grains on the surface and the internal grains. Moreover, a comparative analysis of Al element maps obtained by EDS and CL luminescence feature maps reveals the correlation between the specific CL band and the increased Al concentration. This article comprehensively demonstrates the powerful role of CL in conjunction with other SEM attachments for the analysis of microstructures. Indeed, BSE, EDS and EBSD are well-recognized analytical tools in the metal research domain. However, CL remains relatively unfamiliar to researchers in this field. The integrated application of these instruments in this

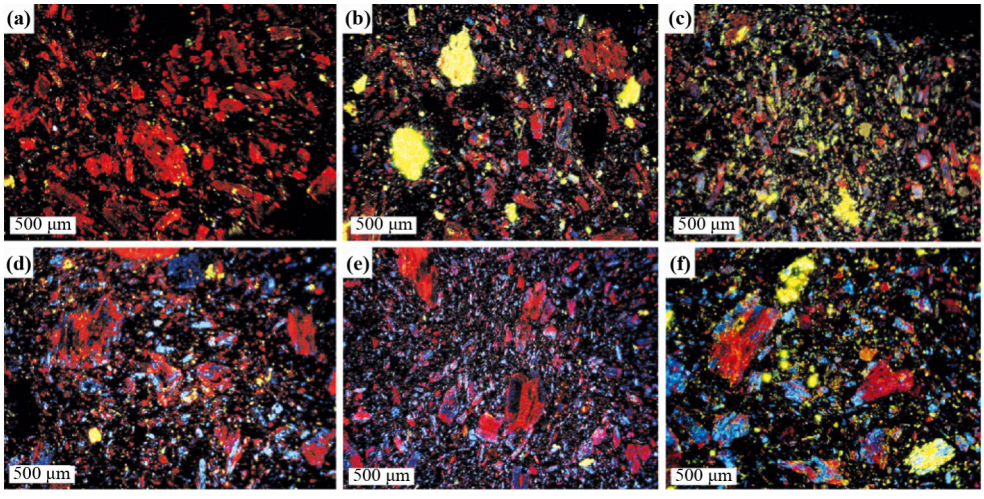

Fig. 3 CL figures: (**a**) category one, with mainly red luminescence; (**b**) category three, with large green luminescent grains; (**c**) category three, with small green luminescing grains; (**d**) category two, with large bicolored grains; (**e**) category two, with numerous small blue luminescing grains; (**f**) category three, with various differently colored grains (see online for a color version of this figure). Reproduced with permission from Ref. [53].

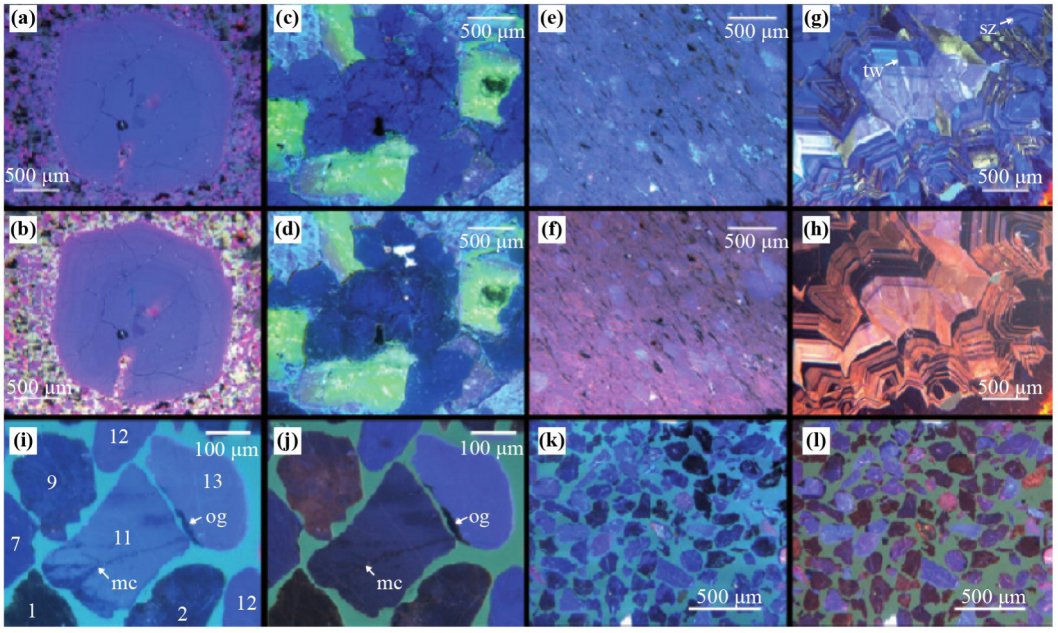

Fig. 4 (**a**) Initial and (**b**) final CL-images of a rhyolithic quartz from Sachsen. (**c**) Initial and (**d**) final CL-images of a granitic quartz from Poland. (**e**) Initial and (**f**) final CL-images of a quartz from the HP-LT-metamorphic rocks of the Peloponnesus. (**g**) Initial and (**h**) final CL-images of a hydrothermal quartz from Wülfrath. (**i**) Initial and (**j**) final CL-images of the Holocene sand sediments of Wangerooge. (**k**) Initial and (**l**) final CL-images of the Lower Cretaceous sands from Ottenstein. Reproduced with permission from Ref. [49].

literature provides an excellent inspiration. Although metallic materials themselves may not emit light, the presence of oxides, inclusions, or certain trace elements within them could exhibit luminescent properties. It is worth considering whether an investigation from the CL perspective could elucidate the impact of oxides on microstructural phenomena such as composition segregation and grain orientation.

4 Applications of SEM-CL in perovskite materials research

In recent years, halide perovskite materials have garnered extensive attention from researchers due to their advantages such as large carrier diffusion lengths, easily tunable bandgap widths, high defect tolerance, low manufacturing costs, and short energy payback periods, demonstrating tremendous commercial potential in the field of photovoltaic materials [54–56]. However, environmental factors such as temperature, humidity, light exposure, or electron irradiation can alter the material, posing significant obstacles to the practical application of halide perovskite solar cells. Phase segregation and ion migration are two major factors contributing to the instability of perovskite materials, which not only alter their local chemical composition and electronic structure but also affect carrier transport and recombination, having a profound impact on the electrical properties of the materials and the performance of the corresponding devices. SEM-CL combines the analysis of material structure, chemical composition, and photoelectric properties in the same micro-region of the sample, playing a crucial role in studying the microstructural evolution of halide perovskite films, including film coverage, flatness, crystal quality, phase separation, and their impacts on local charge transport and optical properties [6].

Duong et al. [15] doped rubidium iodide (RbI) into perovskite films to suppress the formation of PbI_2 and confirmed the variation in the spatial distribution of the PbI_2 phase with the amount of RbI doping using monochromatic imaging with bandpass filtering for both PbI_2 and perovskite phases. The three phases — PbI_2, perovskite, and Rb-rich phase (Fig. 6) — cannot be distinguished by SE morphology, as shown in left panels in Fig. 7. However, their CL properties are distinct; the CL spectra shown in Fig. 6 reveal that the luminescence bands for PbI_2 and perovskite are in the ranges of 505–575 and > 605 nm, respectively. Therefore, monochromatic imaging with specific wavelengths can be

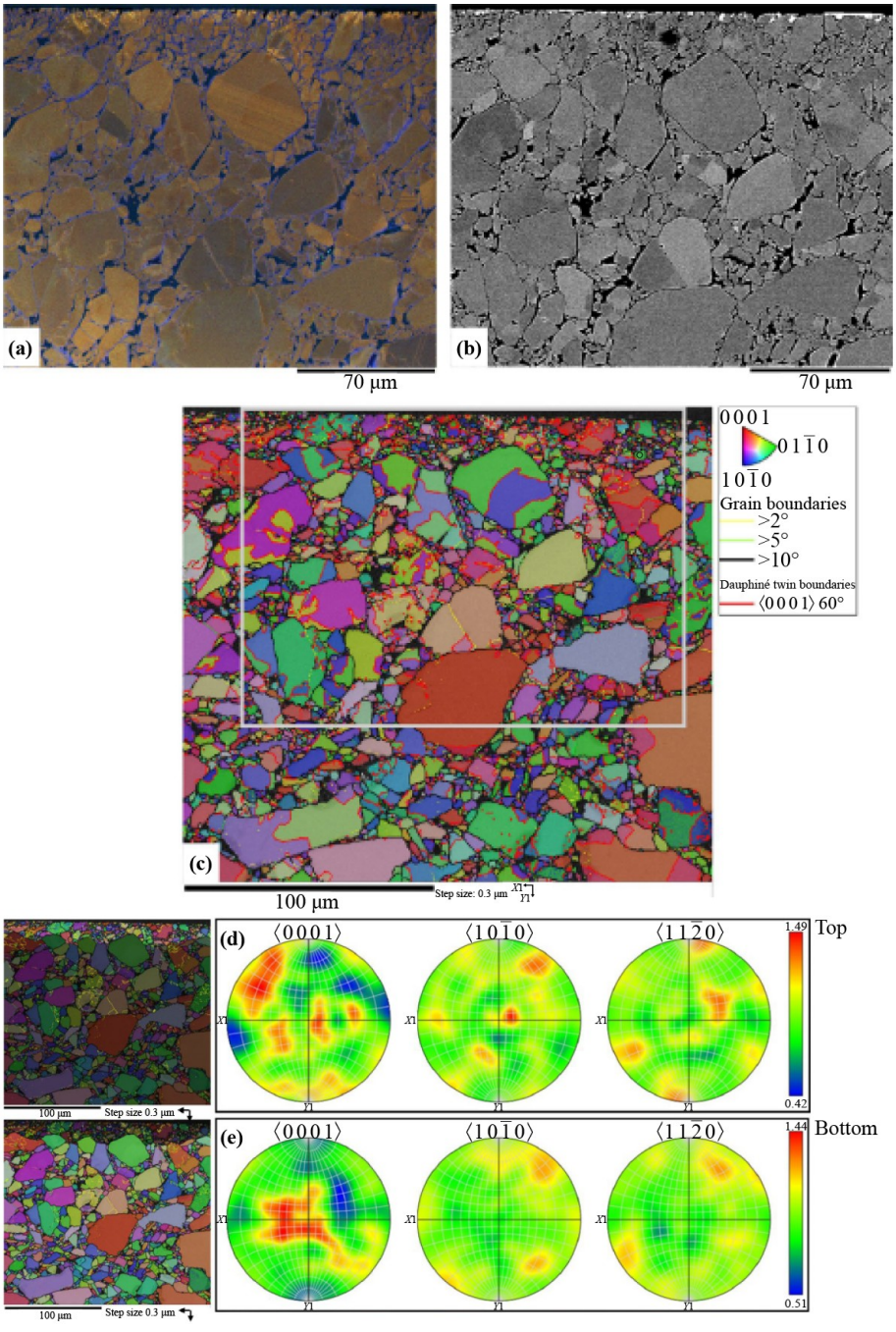

Fig. 5 (**a**) False-color RGB SEM-CL image and (**b**) corresponding BSE image. Shear direction is in the image horizontal (probably top to the left). (**c**) EBSD IPF x map overlay on band contrast map, with grain boundaries (> 10° misorientation) in black, Dauphine twin boundaries (60° rotation around the *c*-axis) in red, low-angle boundaries (5°–10°) in green, and very low-angle boundaries (2°–5°) in yellow. Grey box shows the location of CL and BSE images in Panels (a) and (b). (**d**) Orientation density plot (equal area, lower hemisphere) for the top fine-grained part of the map in Panel (c). (**e**) Orientation density plot (equal area, lower hemisphere) for the rest of the map in Panel (c). Both top and bottom show a low MUD (multiples of uniform distribution) of ~ 1.5, indicating no significant difference in crystal preferred orientation between the top (near the slip surface) and the rest of the sample. *X*1 and *Y*1 in the pole figures in Panels (d) and (e) refer to *X*1 and *Y*1 axes of the EBSD map in Panel (c), respectively, and are in the sample reference system. Reproduced with permission from Ref. [8].

used to selectively image certain luminescent phases, vividly displaying their distribution, as shown in right panels in Fig. 7. This figure compares the PbI_2 phase distribution in perovskite film samples doped with 0%, 5%, and 10% RbI, all containing the same excess of PbI_2. The grains that emit light correspond to the phase with the

selected specific wavelength luminescence; for example, 605 nm corresponds to the perovskite phase, while the non-luminescent grains are the PbI_2 phases. By comparing the same area in the SE images, PbI_2 and Rb-rich phases are circled in green and red, respectively. By contrasting SEM images and CL monochromatic images of samples with different RbI doping levels, the reduction in the spatial distribution of PbI_2 with increasing RbI doping can be observed intuitively and clearly.

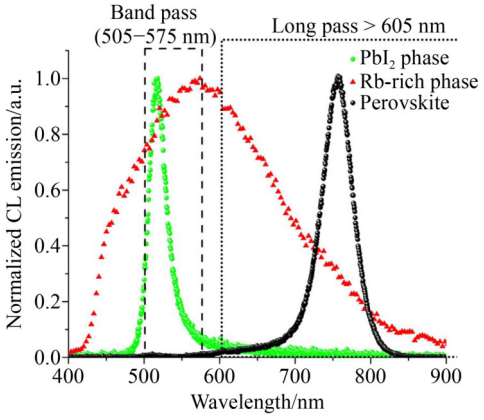

Fig. 6 CL spectra of PbI_2, perovskite, and Rb-rich phases. Reproduced with permission from Ref. [15].

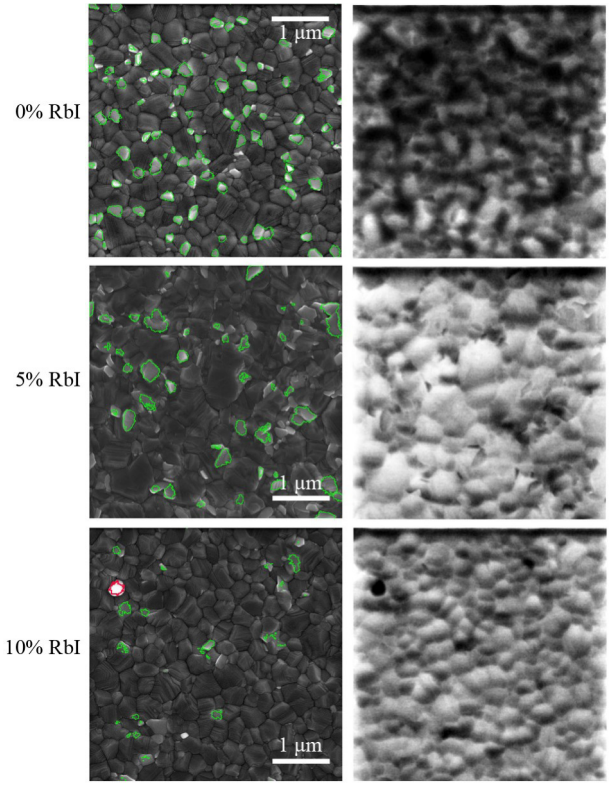

Fig. 7 SEM images of perovskite film with 15% excess PbI_2 and 0%, 5%, and 10% RbI doping (left). CL images of perovskite films on the left picture with a 605 nm long pass filter (right). Reproduced with permission from Ref. [15].

In addition to visually manifesting the characteristics of various phase distributions through monochromatic imaging capabilities within SEM-CL, the distribution features can also be further analyzed to elucidate the process of ion migration. Cortecchia et al. [14] investigated multi-dimensional perovskite films composed of a cation mixture of phenethylamine (PEA) and methylamine (MA). They prepared pure $(PEA)_2PbI_4$, $(PEA)_2(MA)[Pb_2I_7]$, and $MAPbI_3$ crystals, corresponding to compounds in the $(PEA)_2(MA)_{n-1}[Pb_nI_{3n+1}]$ series with $n = 1$, $n = 2$, and $n = \infty$, respectively. Initially, they used CL spectroscopy mode to determine the dominant emission peak wavelengths for samples with $n = 1$, 2, and ∞, as shown in Fig. 8, which were 518, 576, and 780 nm, respectively. Subsequently, they used three bandpass filters for CL single-color imaging to reveal the spatial distribution of the three phases, as shown in Fig. 9. The notable aspect of this article is the authors correlated SE images with luminescence characteristics to elucidate the relationship between ion migration and the formation process of various phases. The SE images revealed that the multi-dimensional films formed plates crystalline, as shown in Fig. 9(a). The plate grain areas were further subdivided into three parts: the grain edge (Point A), the interior of the grain (Point B), and the inter-grain region (Point C). The CL luminescence spectra were collected for these three regions (Fig. 9(f)), and by correlating them with the luminescence spectra of the three phases (Fig. 8(b)), it was determined that the grain edge corresponds to the $n = 1$ phase, the interior of the grain to

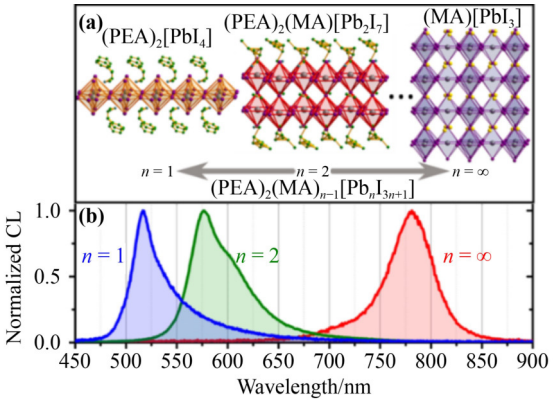

Fig. 8 (**a**) Crystal structures of $(PEA)_2[PbI_4]$, $(PEA)_2(MA)[Pb_2I_7]$, and $MAPbI_3$. (**b**) Corresponding normalized CL spectra. Reproduced with permission from Ref. [14].

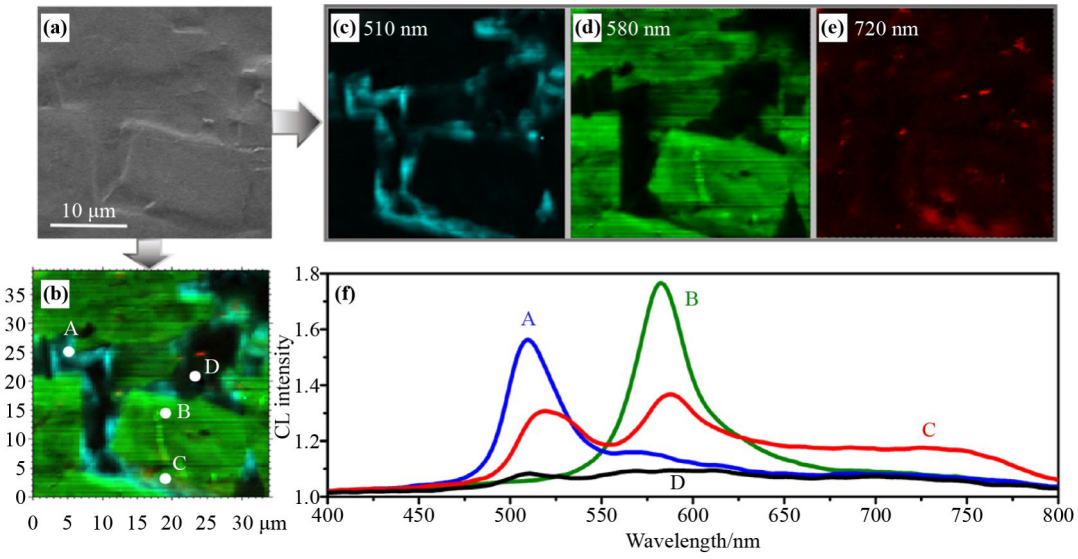

Fig. 9 (**a**) Scanning electron microscopy image of the multiphase $(PEA)_2(MA)_{n-1}[Pb_nI_{3n+1}]$ perovskite film and (**b**) corresponding CL map. (**c**)(**d**)(**e**) Single-color CL maps with components centered at 510, 580, and 720 nm, respectively. (**f**) Spatially resolved CL spectra at specific points of the CL map in Panel (b). Reproduced with permission from Ref. [14].

the $n = 2$ phase, and the inter-grain region to a coexistence of $n = 1$ and $n = 2$ phases, with other areas attributed to the formation of phases with $n \geqslant 3$. Based on this, the authors explained that during the crystallization process of the $n = 2$ perovskite phase, the depletion of MA^+ cations near the grain edges led to the preferential formation of the $n = 1$ phase in that region. The excess MA^+ segregated within the $n = 2$ phase (i.e., the interior of the grains), driving the formation of the higher-dimensional $n = 3$ phase.

Taylor et al. [17] utilized SEM-CL imaging technology to investigate the nanoscale photophysical and degradation processes within individual grains of perovskite. The innovation is particularly pronounced through the supplementation of machine learning by incorporating non-negative matrix factorization (NMF). Initially, the spectral acquisition results from the SEM-CL system were used to determine the luminescence wavelengths corresponding to $MAPbI_3$ and PbI_2 phases at 765 and 510 nm, respectively. Subsequently, SE images of a single large grain, along with monochromatic images filtered for the two wavelengths, were collected, as shown in Fig. 10. The single-color images essentially provided a clear visualization of the phase distribution characteristics. Moreover, in order to separate overlapping spectral signals for further refined study, the researchers introduced NMF to analyze the hyperspectral data collected by CL. NMF decomposes the data into the intensities of spectral images in physical space, decomposing the original data into a large number of subsets to isolate overlapping spectral signals within complex spectral data, thereby clearly revealing the luminescence intensities of the perovskite, PbI_2, and intermediate phases. After NMF-based simulation, an additional signal attributed to the photonic cycle was parsed out. This signal is not actually emitted when the sample is subjected to the electron beam; it may be internalized within the lattice or reabsorbed by adjacent unit cells and the system, as shown in Fig. 11. Combined with CL and NMF analyses, the luminescence characteristics and changes of $MAPbI_3$, PbI_2, and recycled photons under different voltages of 5, 10, and 20 kV are intuitively expressed in the figure. With the increase in acceleration voltage, both the energy deposition depth and the beam-induced damage increase, leading to changes in both spatial intensity maps and spectral shapes. After 10 kV, the entire film has undergone considerable degradation. Subsequent increases in voltage lead to the observation that PbI_2 does not migrate significantly, with luminescence becoming more pronounced, while some regions of the perovskite that previously luminesced do not luminesce anymore due to the degradation after electron beam irradiation.

5 Applications of SEM-CL in semiconductor materials research

Semiconductor materials hold a pivotal role in

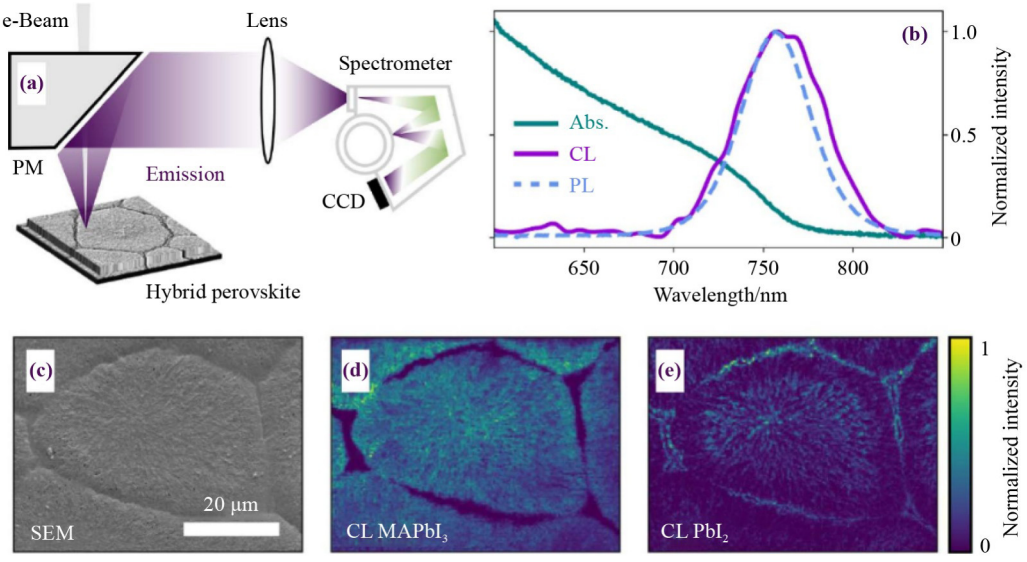

Fig. 10 Overview of CL spectroscopy of large-grain hybrid perovskites: (**a**) schematic of CL setup; (**b**) representative spectra of optical absorption, PL, and CL collected at the center of a grain; (**c**) SEM of a grain; (**d**)(**e**) normalized single-wavelength CL intensity maps of the hybrid perovskite band-edge (λ = 765 nm) (Panel (d)) and the PbI_2 emission (λ = 510 nm) (Panel (e)). Reproduced with permission from Ref. [17].

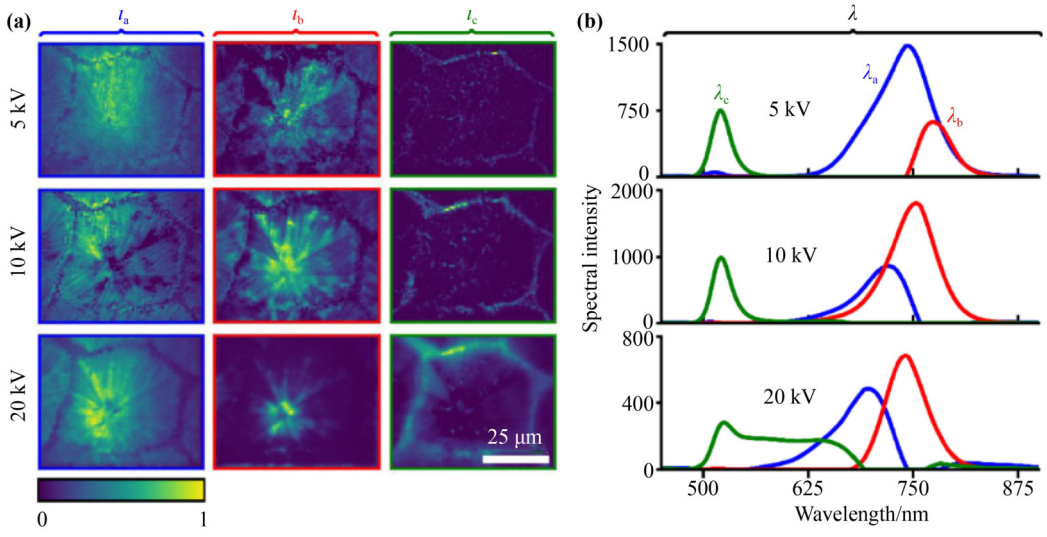

Fig. 11 Blind NMF decomposition of environmentally exposed sample with rank three: (**a**) normalized spatial intensity maps resulting from the NMF decomposition (I_a corresponds to the primary band-edge recombination spatial location, I_b corresponds to the photon recycling, and I_c is the PbI_2 CL); (**b**) spectral vectors which pair to the spatial intensity maps in Panel (a) (as accelerating voltage is increased, the spectral shapes and spatial intensity maps change due to energy deposition depth and beam induced damage). Reproduced with permission from Ref. [17].

luminescent devices due to their controllable band structure, direct bandgap characteristics, high electroluminescence efficiency, and superior energy efficiency. The SEM-CL system offers unique advantages and promising applications for investigating various properties of semiconductor materials at the submicron scale, including defects, band structures, impurities, quantum dots, and crystal quality [19–35].

Guo et al. [20] investigated the lateral polarity junctions in 3D bandgap III-nitride quantum wells, utilizing the SEM-CL system to characterize the luminescent properties of different polarity regions, thereby elucidating how the introduction of lateral polarity junctions enhances radiative recombination. As shown in Fig. 12, the CL spectrum was first used to identify the two primary luminescence peaks of the lateral polarity

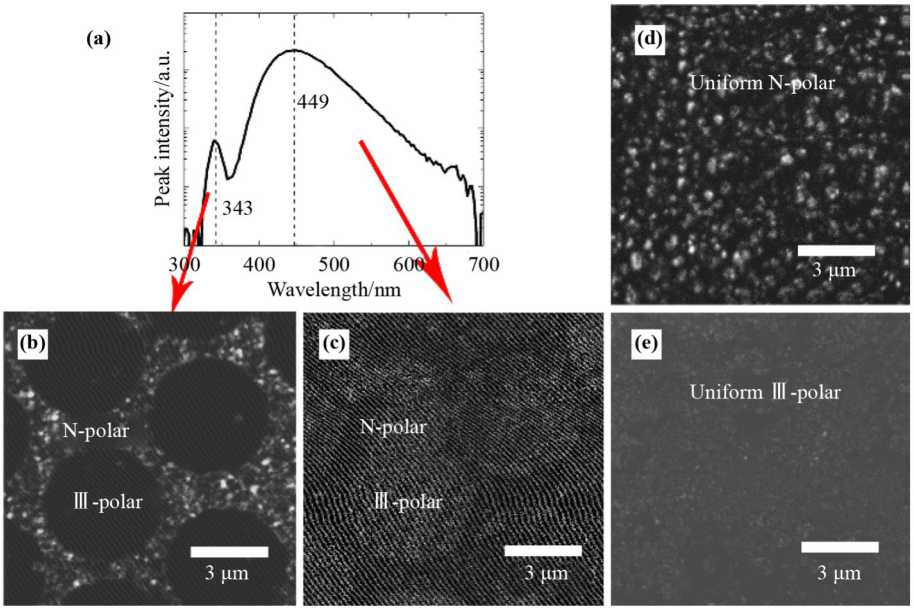

Fig. 12 (**a**) CL spectrum of the lateral polarity junction (LPJ) multiple quantum wells (MQWs). (**b**) Monotonic CL intensity distribution collected at λ = 343 nm. (**c**) Monotonic CL intensity distribution collected at λ = 449 nm. (**d**) Monotonic CL intensity distribution of the uniform N-polar MQW sample collected at λ = 343 nm. (**e**) Monotonic CL intensity distribution of the uniform III-polar MQW samples collected at λ = 343 nm. Reproduced with permission from Ref. [20].

junction multiple quantum wells, which are the quantum well emission at 343 nm and the deep-level emission at 449 nm. Subsequently, CL filtered-wavelength luminescence intensity maps were collected at the wavelengths of these two peaks, as depicted in Figs. 12(b) and 12(c). The maps visually illustrate that the luminescence intensity of the multiple quantum wells is significantly stronger in the N-polarity region than in the III-polarity region. In contrast, the deep-level emission intensity is slightly stronger in the III-polarity region than in the N-polarity region. To further identify the localized luminescent characteristics of multiple quantum wells, CL filtered-wavelength monotonic images were acquired at 343 nm for both the N-polarity and the III-polarity regions, as shown in Figs. 12(d) and 12(e). These images demonstrate that the luminescence in the N-polarity region appears as non-uniform, dot-like features, whereas the luminescence in the III-polarity region is weaker and more uniform.

Dislocations are the primary defects in semiconductor growth. The lattice mismatch and thermal expansion coefficient mismatch between the GaN layer and the substrate will inevitably introduce large strain and a high density of dislocations. Researchers have studied various methods to reduce the dislocation density. Since dislocations are radiation recombination centers and do not emit light in the CL image, the SEM-CL system is a very intuitive tool for studying the dislocation density and types of defects in semiconductors [19,23,26,28–30,33–35]. Besides, the application of the SEM-CL system can also be combined with cross-sectional analysis of the sample to study the growth mechanism of defects in more depth.

Lee et al. [23] studied two types of hexagonal pits in GaN, as shown in Fig. 13. The sharp-bottomed pit is a V-shaped pit composed of six $\{1\,0\,\bar{1}\,1\}$ crystal facets, while the blunt-bottomed pit is a U-shaped pit composed of six $\{1\,0\,\bar{1}\,1\}$ crystal facets and a bottom. In the CL panchromatic image of the same region, the $\{1\,0\,\bar{1}\,1\}$ crystal facets in both V-shaped and U-shaped pits exhibit the highest luminescence intensity, with the luminescence intensity of the bottom of the U-shaped pit being slightly lower. In addition, the distribution of black spots in the image also intuitively presents the characteristics of dislocation distribution. Combined with the CL observation of cross-sectional samples, the mechanism of generation, growth, and annihilation of the two types of pit defects was analyzed. As shown in Fig. 14, there was a flat SE morphology area with a V-shaped pit under CL, and a bundle of transverse dislocations below the pit bottom were also observed. Based on the CL image, combined with the growth rates of different crystal facets, the mechanism of pit generation and annihilation was presented. The growth rates of $(0\,0\,0\,1)$, $(1\,0\,\bar{1}\,1)$, and

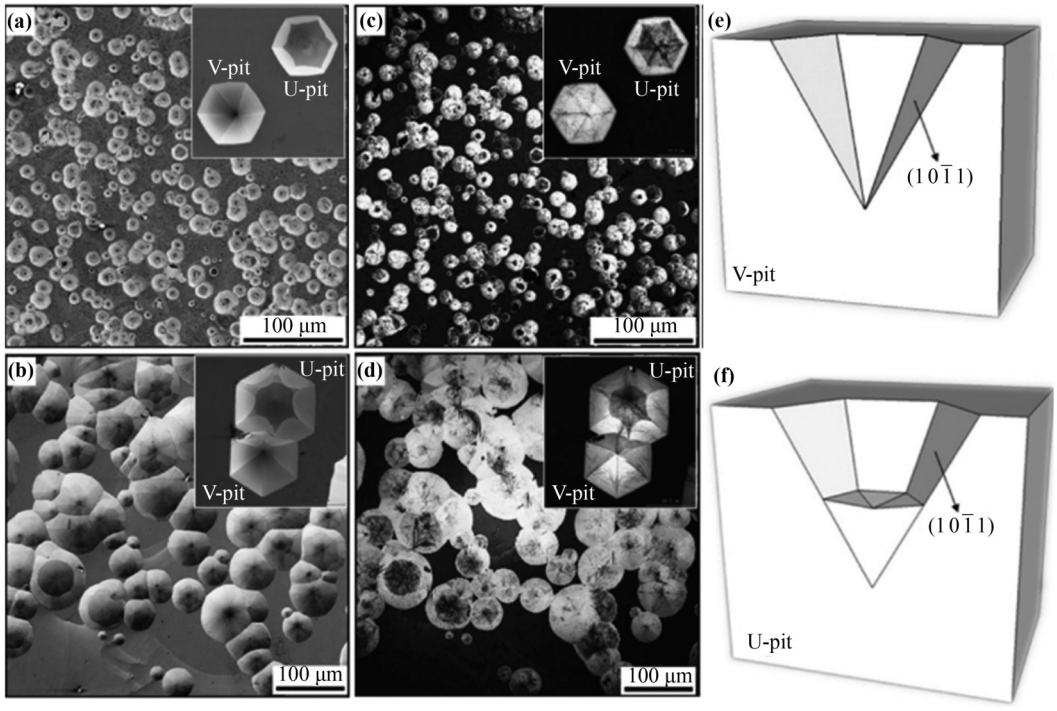

Fig. 13 (**a**)(**b**) SE and (**c**)(**d**) CL images of Samples A and B (the insets are magnified images of V-/U-pits). (**e**)(**f**) 3D schematic drawings of V-pit (Panel (e)) and U-pit (Panel (f)). Reproduced with permission from Ref. [23].

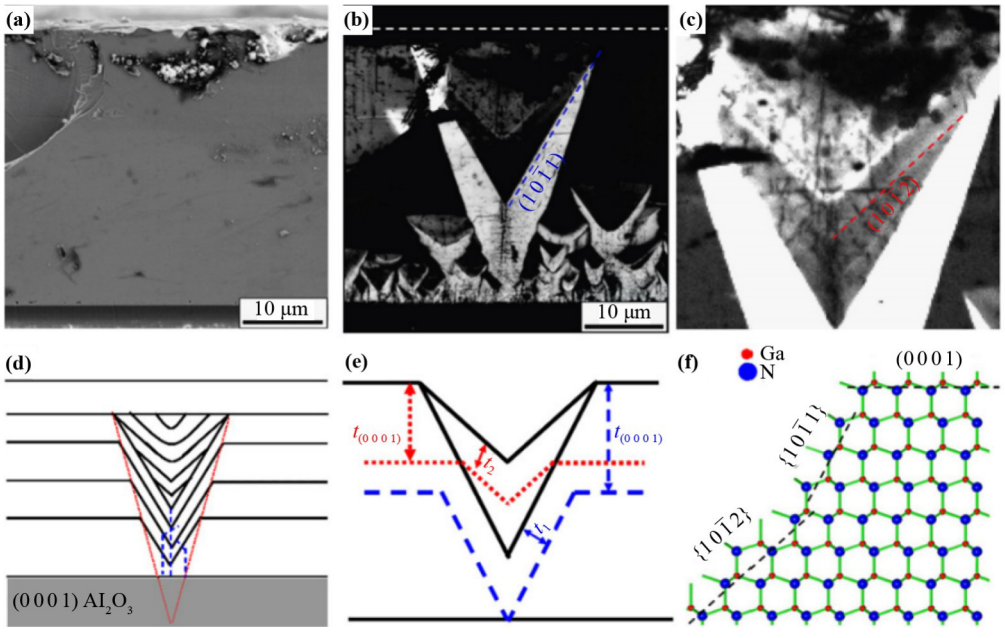

Fig. 14 (**a**)(**b**) Cross-sectional SE image (Panel (a)) and CL image (Panel (b)). (**c**) CL image of a filled region with higher brightness. (**d**)(**e**)(**f**) Schematic drawings of pit growth and annihilation (Panel (d)), growth thickness along each facet (t_1 and t_2 are for {1 0 $\bar{1}$ 1} and {1 0 $\bar{1}$ 2} facets, respectively) (Panel (e)), and atomic arrangement in the [1 $\bar{2}$ 1 0] projection (Panel (f)). Reproduced with permission from Ref. [23].

(1 0 $\bar{1}$ 2) crystal facets are 1:0.38:0.19, respectively. After the dislocation bundle is formed, the growth of the GaN (0 0 0 1) facet is inhibited, resulting in the formation of (1 0 $\bar{1}$ 1) crystal facet steps around the dislocation bundle. Since the growth rate of the (1 0 $\bar{1}$ 1) crystal facet is slower, the V-shaped pit grows larger. As the growth continues, when the V-shaped pit bottom forms connected (1 0 $\bar{1}$ 2) crystal facets, it transforms into a U-shaped pit.

Due to the faster growth rate of the $(1\ 0\ \bar{1}\ 2)$ crystal facet, such filling continues until the V-shaped pit is completely filled, leading to pit annihilation.

6 Application of SEM-CL in identification of non-metallic inclusions in metallic materials

Metals are generally not considered to be luminescent materials, hence researchers in the metal field are often unfamiliar with the SEM-CL system, and its application in materials research is even less common. While metals do not emit light themselves, the microscopic defects within them, such as cracks, pores, and inclusions, can be excited by high-speed electrons to produce specific luminescence signals from atomic structures surrounding these defects. These signals can be useful for analyzing and identifying the nature of defects.

Non-metallic inclusions in metallic materials can lead to various defects, such as fracture, hydrogen-induced cracking, fatigue failure, surface defects, and low-temperature embrittlement, which significantly reduce the material's mechanical properties, fatigue life, and durability [57–59]. Therefore, the identification of the size distribution, shape, and chemical composition of non-metallic inclusions in steel, iron, and copper is of great importance. OM and electron probe microanalysis (EPMA) are commonly adopted for identifying inclusions in steel, but these methods are time-consuming. The SEM-CL system enables the simultaneous acquisition of images and spectra of sample micro-regions, providing a unique method for the rapid identification of the quantity, size distribution, shape, and composition of non-metallic inclusions in steel [36–40].

While EDS and EPMA are commonly used to detect the distribution and concentrations of elements in micro-regions of metal materials, the knowledge of element types does not necessarily determine the phase, especially when the elemental composition is complex or concentrations of certain trace elements are below the detection limit of EDS. CL spectroscopy can effectively address this limitation by identifying phases through luminescent characteristics, in conjunction with elemental composition. Imashuku et al. [39] adopted the SEM-CL method to rapidly distinguish between BN and AlN inclusions in metal materials. Figure 15 shows CL image, SEM image, and EPMA mapping of Al, N, and O elements in the same micro-region of the sample. The element mapping reveals that inclusion 3 contains Al, N, and a small amount of O, while inclusion 4 contains Al and O. The elemental composition of inclusion 4 is simple, suggesting its primary Al_2O_3 phase, but the phase of inclusion 3 is difficult to determine. The CL spectra of both inclusions show that inclusion 3 emits blue light and inclusion 4 emits pinkish-white light, as shown in Fig. 16. Inclusion 3 exhibits a luminescent peak at 400 nm, which is consistent with the AlN luminescence peak, confirming that inclusion 3 is of the AlN phase. The CL spectrum of inclusion 4 shows broad peaks near 545 and 740 nm, which are consistent with the luminescence peaks of Al_2O_3, confirming that inclusion 4 is indeed Al_2O_3 phase, in agreement with the EDS analysis.

When inclusions with similar morphologies and

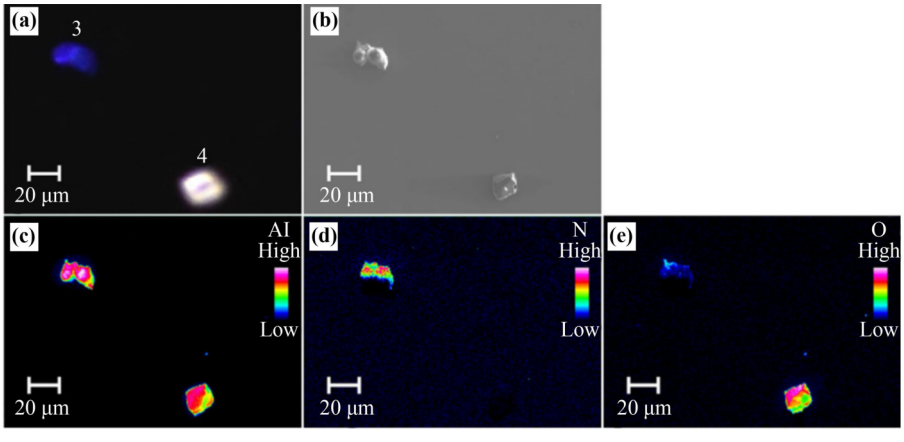

Fig. 15 (**a**) CL image, (**b**) SEM image, and (**c**)(**d**)(**e**) WDX elemental maps for Al (Panel (c)), N (Panel (d)), and O (Panel (e)) on polished surface of the steel sample prepared through heating mixture of Fe and Al powders at 1550 °C in nitrogen atmosphere. Reproduced with permission from Ref. [39].

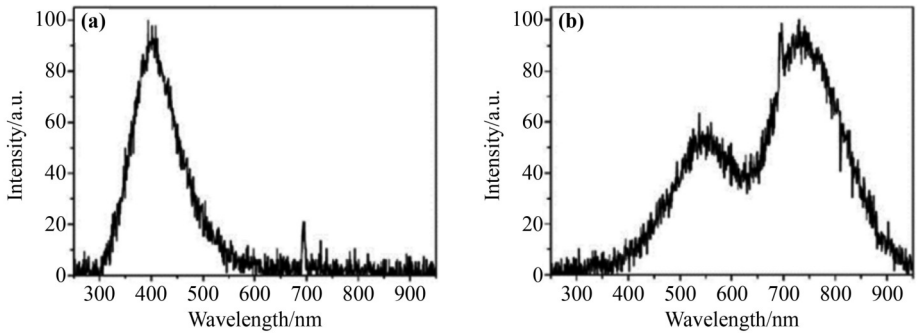

Fig. 16 CL spectra of (**a**) inclusion 3 and (**b**) inclusion 4. Reproduced with permission from Ref. [39].

uniform elemental distributions are present, it is very easy to misjudge them as a single type of inclusion, leading to misleading assessments. CL spectroscopy can effectively avoid such errors [37]. As shown in Fig. 17, the SE image depicts a cluster of inclusions with a uniform appearance, and the EDS mapping results also show a uniform distribution of Al and Mg elements. However, the CL image clearly distinguishes two distinct luminescent colors, with a blue outer ring and a green inner ring, indicating that the inclusion is composed of more than two components. Quantitative EDS analyses were performed on the areas emitting green and blue light in the CL image, as shown in Fig. 18. Although the main components of both regions are Mg, Al, and O elements, the intensity ratio of Al to Mg is different. The intensity ratio of Al to Mg in the green luminescence region matches well with the intensity ratio of $MgAl_2O_4$ spinel, as shown in Fig. 18(c). Therefore, it is inferred that this region be composed of $MgAl_2O_4$ spinel. The blue luminescence region is speculated to be composed of Al_2O_3 and MgO, which have similar luminescence colors. In another work, the team also proposed a method to identify calcium aluminate inclusions in calcium-treated aluminum-killed steel by SEM-CL system [38]. The inclusions of $Ca_{12}Al_{14}O_{33}$, $CaAl_4O_7$, $CaAl_{12}O_{19}$, and Al_2O_3 differ from those of $CaAl_2O_4$ and $Ca_3Al_{10}O_{18}$. Although their compositions are similar, the latter ones do not cause nozzle clogging and stopper melting.

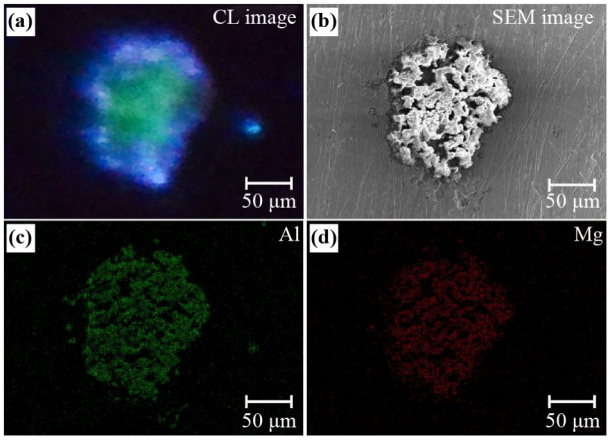

Fig. 17 (**a**) CL image, (**b**) SEM image, and (**c**)(**d**) EDX elemental mappings of Al (Panel (c)) and Mg (Panel (d)) in another area of the surface of the model sample prepared through heating a mixture of Fe, Al, and MgO powders at 1560 °C in argon atmosphere (for interpretation of the references to color in this figure, the reader is referred to the web version of this article). Reproduced with permission from Ref. [37].

7 Applications of SEM-CL in functional ceramic research

Ceramic materials with luminescent properties can be fabricated through doping and special processing techniques. For such luminescent ceramics, the SEM-CL system plays a crucial role in investigating the relationship between their microstructure and luminescent performance [41–46,60].

Rare-earth ion-doped luminescent composite ceramics have wide applications in the field of white light diodes. Due to the low energy level of the rare-earth cerium ion (Ce^{3+}) that can achieve the 4f–5d transition, Ce^{3+} is often doped to study luminescence properties of materials. The relationship among the doping amount of Ce^{3+}, the sintering temperature, the luminescence intensity, and the luminescence efficiency of the material is a key focus of research [45].

Analyses of luminescence images obtained from SEM-CL offer a convenient way to visually compare the luminescence intensity in the micro-regions of the sample, providing a useful function for comparing luminescence

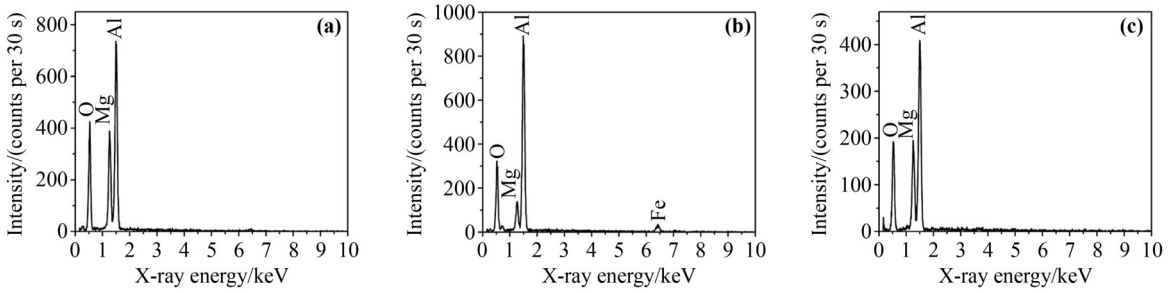

Fig. 18 (**a**)(**b**) EDS spectra of areas producing green (center) luminescence (Panel (a)) and blue (shell) luminescence (Panel (b)) in Fig. 8(a). (**c**) EDS spectrum of the $MgAl_2O_4$ reagent. For interpretation of the references to color in this figure legend, the reader is referred to the web version of this article. Reproduced with permission from Ref. [37].

intensities in the study of luminescent ceramics. Yao et al. [45] optimized YAG:Ce^{3+} transparent luminescent ceramics by adding MgO and SiO_2 and annealing in air to control defects and crystal fields, significantly improving the quality and performance of the ceramics and enhancing the conversion efficiency from blue to white light. Furthermore, the SEM-CL system was employed to examine the correlation between the distribution characteristics of Ce^{3+} ions and the luminescent properties at grain boundaries and defects, as illustrated in Fig. 19. The luminescence is very strong within grains while weak in defects. The luminescence at 540 nm is produced by Ce^{3+} ions in the matrix, and the CL spectrum of Point 1 in the grain exhibits a significantly higher peak intensity than those of Points 2, 3, and 4 at defects.

To further determine the distribution of Ce^{3+}, CL spectral line scans were conducted across the grain and grain boundaries. It was found that the CL intensity in the grain was brighter and stronger than those at grain boundaries, indicating that Ce^{3+} was primarily distributed within the grains rather than at the grain boundaries.

Barium strontium titanate ($Ba_xSr_{1-x}TiO_3$, BST) has garnered significant attention due to its high dielectric constant, low dielectric loss, tunable Curie temperature, and high tunability of dielectric behaviors, which has wide applications in dynamic random access memories (DRAMs), dielectric capacitors, microwave phase shifters, transducers, positive temperature coefficient (PTC) resistors, and energy storage ceramics.

Zhu et al. [46] observed a novel core–shell structure in Bi-doped $Sr_{0.8}Ba_{0.2}TiO_3$ ceramics and utilized SEM-CL to investigate the point defect characteristics of this core–shell structure. One highlight of this literature is that the researchers did not confine themselves to the limited wavelength resolution of the CL spectral peaks but instead performed Gaussian peak decomposition fitting to enhance the accuracy and reliability of the results. The BSE image of the core–shell structure grain is shown in Fig. 20(c). The CL spectra of the core, the rim′, and the rim″ reveal that all three exhibit two distinct broadened peaks in the range of 300–800 nm, as shown in Fig. 20(a). After Gaussian peak fitting, three fitting peaks located around 420 nm (2.9 eV), 515 nm (2.4 eV), and 635 nm (2.0 eV) were obtained, labeled as Peaks I, II, and III, respectively, as shown in Fig. 20(b). Further CL monochromatic images corresponding to the fitted Peaks I, II, and III were collected, as shown in Figs. 20(d)–20(f). It can be intuitively observed that Peak I at 420 nm emits the strongest light in the core region, Peak II at 515 nm emits the highest intensity of light in the edge region, and Peak III emits more strongly in the core region.

Based on these results, the authors also discussed luminescence mechanisms of the three peaks, which may be caused by optical transitions between the interstitial energy levels formed by doping in a reducing atmosphere during sintering. The CL spectrum has three main optical emission peaks at 2.9, 2.4, and 2.0 eV, in which the 2.9 eV peak is caused by oxygen vacancies and the Nb doping, the 2.4 eV peak by charge transfer between Ti^{4+} and O^{2-}, and the 2.0 eV peak by oxygen vacancies and strontium vacancies, which are influenced by the Bi content.

8 Conclusions and prospection

1) When the CL spectrometer is installed on a SEM, it can be combined with other functional attachments to enable the analysis of various characteristics such as high spatial resolution morphology observation, luminescent properties, micro-regional elemental composition, and crystal structure, demonstrating significant potential in the

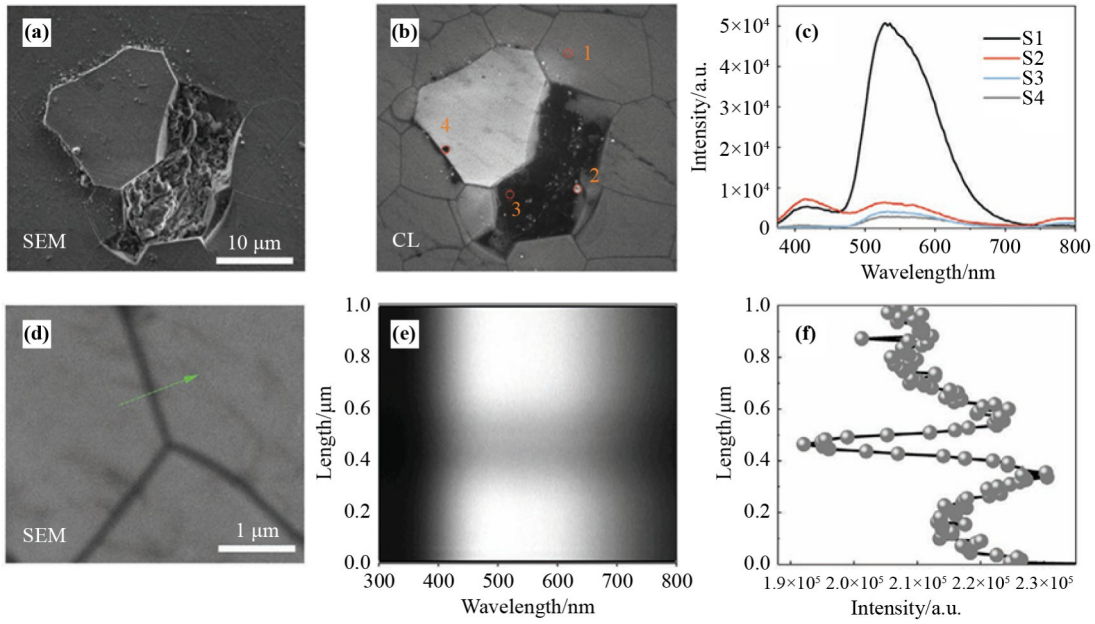

Fig. 19 (**a**) SEM and (**b**) CL images of defects in ceramic. (**c**) CL spectra for Points 1–4 in Panel (b). (**d**) The position of CL line-scan crossing grains and the grain boundary, as indicated by the arrow on the SEM image. (**e**) Line-scan CL spectra for the arrow in Panel (d). (**f**) CL peak intensities along the arrow. Reproduced with permission from Ref. [45].

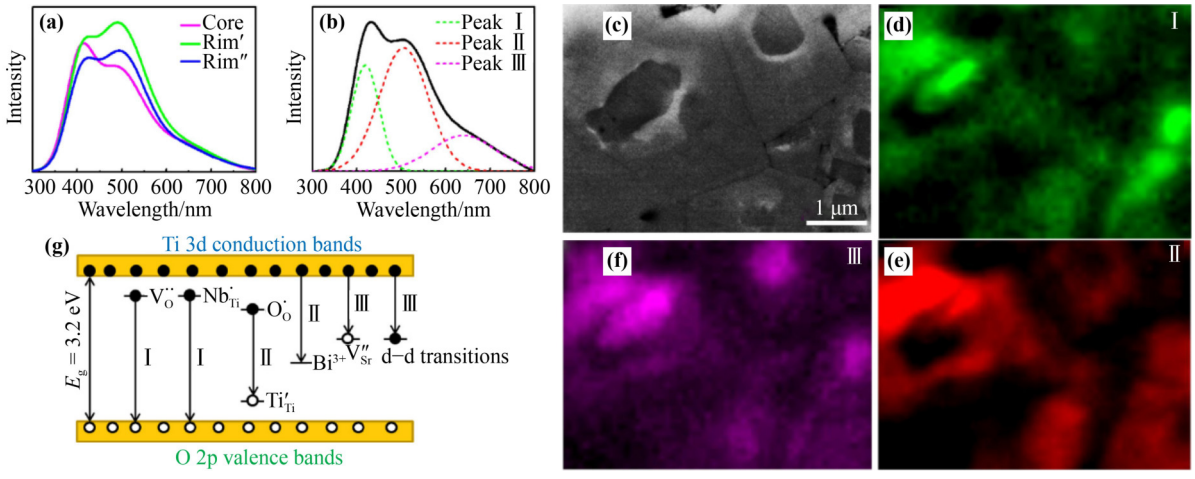

Fig. 20 (**a**) Measured CL spectra of a typical core–rim grain. (**b**) Fitted results with three Gaussian peaks. (**c**)(**d**)(**e**)(**f**) BSE image and corresponding CL maps of fitted Peaks I, II, and III. (**g**) Possible mechanisms for the luminescence emission. Reproduced with permission from Ref. [46].

characterization of material microstructures.

2) When characterizing halide perovskite materials, SEM-CL requires special attention to the electron beam irradiation damage of samples, as perovskites are prone to degradation. Strict control is necessary for voltage, beam current, and acquisition time.

3) SEM-CL analysis of luminescence properties on a microscopic scale breaks through the limitations of traditional photoluminescence and absorption spectroscopy. However, due to the thicker sample size in SEM, the interaction area of the electron beam with the sample is relatively large, and the excitation depth of the CL signal is deeper than that of SE, BSE, and characteristic X-ray signals. For smaller-scale analysis of luminescence performance and band structure, a transmission electron microscope (TEM)-CL system can be employed.

4) The broad energy range of the electron beam in SEM-CL systems often results in a broader spectrum compared to photoluminescence. Therefore, it is

important to use Gaussian peak fitting to determine the exact luminescence peak positions more accurately. In the expression of analysis results, the luminescence wavelength and bandgap energy can be converted.

5) Some references indicate that CL has unique applications in the research of nanomaterials. Nanomaterials are classified based on the size of the sample structure and can encompass a variety of materials. The materials mentioned in this article, such as semiconductors and oxide ceramics, include nanomaterials in terms of material scale [21,60–62].

6) The SEM-CL system has potential applications in the field of pharmaceutical research, such as the structural analysis of drug crystals, purity testing, and imaging of cells and tissues [63]. However, due to the requirement for specialized equipment and techniques, and the ease with which samples can be damaged by the electron beam, it is not as widely used as other fluorescence techniques (such as fluorescence microscopy and confocal microscopy).

Declaration of competing interests The authors declare that they have no conflict of interest.

Acknowledgements The authors are grateful for financial supports by the Zhejiang Provincial Natural Science Foundation (Grant No. TGC24E020003).

References

[1] Coenen T, Haegel N M. Cathodoluminescence for the 21st century: learning more from light. Applied Physics Reviews, 2017, 4(3): 031103

[2] Parish C M, Russell P E. Scanning cathodoluminescence microscopy. Advances in Imaging and Electron Physics, 2007, 147: 1−135

[3] García de Abajo F J. Optical excitations in electron microscopy. Reviews of Modern Physics, 2010, 82(1): 209−275

[4] Kuttge M, Vesseur E J R, Koenderink A F, et al. Local density of states, spectrum, and far-field interference of surface plasmon polaritons probed by cathodoluminescence. Physical Review B: Condensed Matter and Materials Physics, 2009, 79(11): 113405

[5] Frelinger S N, Ledvina M D, Kyle J R, et al. Scanning electron microscopy cathodoluminescence of quartz: principles, techniques and applications in ore geology. Ore Geology Reviews, 2015, 65: 840−852

[6] Guthrey H, Moseley J. A review and perspective on cathodoluminescence analysis of halide perovskites. Advanced Energy Materials, 2020, 10(26): 1903840

[7] Bernet M, Bassett K. Provenance analysis by single-quartz-grain SEM-CL/optical microscopy. Journal of Sedimentary Research, 2005, 75(3): 492−500

[8] Hamers M F, Niemeijer A R, Drury M R. Cathodoluminescence as a tracing technique for quartz precipitation in low velocity shear experiments. Scientific Reports, 2023, 13(1): 10236

[9] Hunt A M W. Development of quartz cathodoluminescence for the geological grouping of archaeological ceramics: firing effects and data analysis. Journal of Archaeological Science, 2013, 40(7): 2902−2912

[10] Imashuku S, Wagatsuma K. Rapid identification of rare earth element bearing minerals in ores by cathodoluminescence method. Minerals Engineering, 2020, 151: 106317

[11] Müller A, Wiedenbeck M, Van Den Kerkhof A M, et al. Trace elements in quartz — a combined electron microprobe, secondary ion mass spectrometry, laser-ablation ICP-MS, and cathodoluminescence study. European Journal of Mineralogy, 2003, 15(4): 747−763

[12] Okumura T, Nishido H, Toyoda S, et al. Evaluation of radiation-damage halos in quartz by cathodoluminescence as a geochronological tool. Quaternary Geochronology, 2008, 3(4): 342−345

[13] Simon K, Scherer T, Van Den Kerkhof A M, et al. Fluid-controlled quartz recovery in granulite as revealed by cathodoluminescence and trace element analysis (Bamble sector, Norway). Contributions to Mineralogy and Petrology, 2004, 146(5): 637−652

[14] Cortecchia D, Lew K C, So J K, et al. Cathodoluminescence of self-organized heterogeneous phases in multidimensional perovskite thin films. Chemistry of Materials, 2017, 29(23): 10088−10094

[15] Duong T, Mulmudi H K, Shen H P, et al. Structural engineering using rubidium iodide as a dopant under excess lead iodide conditions for high efficiency and stable perovskites. Nano Energy, 2016, 30: 330−340

[16] Neher R A, Mitkovski M, Kirchhoff F, et al. Blind source separation techniques for the decomposition of multiply labeled fluorescence images. Biophysical Journal, 2009, 96(9): 3791−3800

[17] Taylor E J, Iyer V, Dhami B S, et al. Hyperspectral mapping of nanoscale photophysics and degradation processes in hybrid perovskite at the single grain level. Nanoscale Advances, 2023, 5(18): 4687−4695

[18] Wang P Y, Meng M M, Nie M, et al. Fabrication of highly stable $Cs_3Cu_2I_5$-in-glass composite for X-ray imaging by SPS technique. Advanced Optical Materials, 2024, 12(21): 2400813

[19] Chen Q S, Gao J H, Chen C, et al. Evolution of dislocations and strains in AlN grown by high-temperature metal–organic chemical vapor deposition. Crystal Growth & Design, 2024,

24(4): 1784−1791

[20] Guo W, Mitra S, Jiang J A, et al. Three-dimensional band diagram in lateral polarity junction III-nitride heterostructures. Optica, 2019, 6(8): 1058−1062

[21] Gustafsson A. Nanowire-based structures for infrared to ultraviolet emitters studied by cathodoluminescence. Journal of Microscopy, 2016, 262(2): 134−141

[22] Hou M J, Qin Z X, Zhang L S, et al. Excitonic localization at macrostep edges in AlGaN/AlGaN multiple quantum wells. Superlattices and Microstructures, 2017, 104: 397−401

[23] Lee W, Lee H J, Park S H, et al. Cross sectional CL study of the growth and annihilation of pit type defects in HVPE grown (0 0 0 1) thick GaN. Journal of Crystal Growth, 2012, 351(1): 83−87

[24] Liu Z X, Jiang M L, Hu Y L, et al. Scanning cathodoluminescence microscopy: applications in semiconductor and metallic nanostructures. Opto-Electronic Advances, 2018, 1(4): 180007

[25] Loeto K, Kusch G, Ghosh S, et al. Quantitative analysis of carbon impurity concentrations in GaN epilayers by cathodoluminescence. Micron, 2023, 172: 103489

[26] Meissner E, Schweigard S, Friedrich J, et al. Cathodoluminescence imaging for the determination of dislocation density in differently doped HVPE GaN. Journal of Crystal Growth, 2012, 340(1): 78−82

[27] Metzner S, Bertram F, Karbaum C, et al. Spectrally and time-resolved cathodoluminescence microscopy of semipolar InGaN SQW on (1 1 $\bar{2}$ 2) and (1 0 $\bar{1}$ 1) pyramid facets. physica status solidi (b), 2011, 248(3): 632−637

[28] Ngo T H, Comyn R, Frayssinet E, et al. Cathodoluminescence and electrical study of vertical GaN-on-GaN Schottky diodes with dislocation clusters. Journal of Crystal Growth, 2020, 552: 125911

[29] Pauc N, Phillips M R, Aimez V, et al. Carrier diffusion processes near threading dislocations in GaN and GaN:Si characterized by low voltage cathodoluminescence. Superlattices and Microstructures, 2006, 40(4−6): 557−561

[30] Sekiguchi T, Lee W, Luo X J, et al. Cathodoluminescence study of killer defects in GaN wafers on sapphire substrates. physica status solidi (c), 2017, 14(7): 1700054

[31] Sheikhi M, Dai Y J, Cui M, et al. On the luminescence properties and surface passivation mechanism of III- and N-polar nanopillar ultraviolet multiple-quantum-well light emitting diodes. Micromachines, 2020, 11(6): 572

[32] Sutherland D, Zhu T T, Griffiths J T, et al. Optical studies of non-polar m-plane (1 $\bar{1}$ 0 0) InGaN/GaN multi-quantum wells grown on freestanding bulk GaN. physica status solidi (b), 2015, 252(5): 965−970

[33] Wang J, Oshima Y, Cho Y, et al. Cathodoluminescence study on the impurity behaviors at threading dislocations in GaN. Superlattices and Microstructures, 2016, 99: 77−82

[34] Yao Y, Ishikawa Y, Sudo M, et al. Characterization of threading dislocations in GaN (0 0 0 1) substrates by photoluminescence imaging, cathodoluminescence mapping and etch pits. Journal of Crystal Growth, 2017, 468: 484−488

[35] Yao Y, Ishikawa Y, Sugawara Y, et al. Revelation of dislocations in HVPE GaN single crystal by KOH etching with Na_2O_2 additive and cathodoluminescence mapping. Superlattices and Microstructures, 2016, 99: 83−87

[36] Imashuku S, Ono K, Wagatsuma K. Rapid phase mapping in heat-treated powder mixture of alumina and magnesia utilizing cathodoluminescence. X-Ray Spectrometry, 2017, 46(2): 131−135

[37] Imashuku S, Ono K, Shishido R, et al. Cathodoluminescence analysis for rapid identification of alumina and $MgAl_2O_4$ spinel inclusions in steels. Materials Characterization, 2017, 131: 210−216

[38] Imashuku S, Wagatsuma K. Rapid identification of calcium aluminate inclusions in steels using cathodoluminescence analysis. Metallurgical and Materials Transactions B: Process Metallurgy and Materials Processing Science, 2018, 49(5): 2868−2874

[39] Imashuku S, Wagatsuma K. Cathodoluminescence analysis of nonmetallic inclusions of nitrides in steel. Surface and Interface Analysis, 2019, 51(1): 31−34

[40] Tribaudino M, Bersani D, Mantovani L, et al. Cathodoluminescence, Raman and scanning electron microscopy with energy dispersion system mapping to unravel the mineralogy and texture of an altered Ca–Al-rich inclusion in Renazzo CR2 carbonaceous chondrite. Journal of Raman Spectroscopy, 2021, 52(11): 1892−1901

[41] Chiang T Y, Tsai C H, Huang M C, et al. Cathodoluminescence study of defects in thermal treatment of zinc titanate thin films deposited by a cosputtering process. Surface and Interface Analysis, 2018, 50(5): 541−546

[42] Ihrig H, Hengst J, Klerk M. Conductivity-dependent cathodoluminescence in $BaTiO_3$, $SrTiO_3$ and TiO_2. Zeitschrift für Physik B: Condensed Matter, 1981, 40(4): 301−306

[43] Nishi M, Tanabe S, Fujita K, et al. Phase-selective cathodoluminescence spectroscopy of Er:YAG glass-ceramics. Solid State Communications, 2004, 132(1): 19−23

[44] Yang K H, Chen T Y, Ho N J, et al. In-gap states in wide-band-gap $SrTiO_3$ analyzed by cathodoluminescence. Journal of the American Ceramic Society, 2011, 94(6): 1811−1816

[45] Yao Q, Hu P, Sun P, et al. YAG:Ce^{3+} transparent ceramic phosphors brighten the next-generation laser-driven lighting.

Advanced Materials, 2020, 32(19): 1907888

[46] Zhu S Y, Li J, Xing J J, et al. Cathodoluminescence characteristics of a novel core–rim structure in Bi-doped (Sr,Ba)TiO_3 ceramics. Ceramics International, 2019, 45(6): 8027−8031

[47] Coenen T, Vesseur E J R, Polman A. Angle-resolved cathodoluminescence spectroscopy. Applied Physics Letters, 2011, 99(14): 143103

[48] Vesseur E J R, Coenen T, Caglayan H, et al. Experimental verification of $n = 0$ structures for visible light. Physical Review Letters, 2013, 110(1): 013902

[49] Götte T, Richter D K. Cathodoluminescence characterization of quartz particles in mature arenites. Sedimentology, 2006, 53(6): 1347−1359

[50] Götze J, Plötze M, Habermann D. Origin, spectral characteristics and practical applications of the cathodoluminescence (CL) of quartz — a review. Mineralogy and Petrology, 2001, 71(3−4): 225−250

[51] Mavris C, Götze J, Plötze M, et al. Weathering and mineralogical evolution in a high Alpine soil chronosequence: a combined approach using SEM–EDX, cathodoluminescence and Nomarski DIC microscopy. Sedimentary Geology, 2012, 280: 108−118

[52] Omer M F, Omer D, Zebari B G. High resolution cathodoluminescence spectroscopy of carbonate cementation in Khurmala Formation (Paleocene–L. Eocene) from Iraqi Kurdistan Region, Northern Iraq. Journal of African Earth Sciences, 2014, 100: 243−258

[53] Weiss C, Köster M, Japp S. Preliminary characterization of pottery by cathodoluminescence and SEM–EDX analyses: an example from the Yeha Region (Ethiopia). Archaeometry, 2016, 58(2): 239−254

[54] Ansari M I H, Qurashi A, Nazeeruddin M K. Frontiers, opportunities, and challenges in perovskite solar cells: a critical review. Journal of Photochemistry and Photobiology C: Photochemistry Reviews, 2018, 35: 1−24

[55] Burschka J, Pellet N, Moon S J, et al. Sequential deposition as a route to high-performance perovskite-sensitized solar cells. Nature, 2013, 499(7458): 316−319

[56] Kim H S, Lee C R, Im J H, et al. Lead iodide perovskite sensitized all-solid-state submicron thin film mesoscopic solar cell with efficiency exceeding 9%. Scientific Reports, 2012, 2(1): 591

[57] Harada A, Miyano G, Maruoka N, et al. Dissolution behavior of Mg from MgO into molten steel deoxidized by Al. ISIJ International, 2014, 54(10): 2230−2238

[58] Okuyama G, Yamaguchi K, Takeuchi S, et al. Effect of slag composition on the kinetics of formation of Al_2O_3–MgO inclusions in aluminum killed ferritic stainless steel. ISIJ International, 2000, 40(2): 121−128

[59] Hyun P J, Todoroki H. Control of $MgO{\cdot}Al_2O_3$ Spinel inclusions in stainless steels. ISIJ International, 2010, 50(10): 1333−1346

[60] Zhu L C, Lockrey M, Phillips M R, et al. Spatial distribution of defect luminescence in ZnO nanorods: an investigation by spectral cathodoluminescence imaging. physica status solidi (a), 2018, 215(19): 1800389

[61] Ghosh K, Ghorai G, Sahoo P K. Cathodoluminescence and structural properties of ZnTe nanocrystals synthesized from Te/ZnO thin films. Journal of Alloys and Compounds, 2023, 960: 170655

[62] He X, Liu D L, Dang Z B, et al. Super-resolved bulk states of photonic crystals with cathodoluminescence microscopy. Laser & Photonics Reviews, 2023, 17(9): 2200818

[63] Nichols G. Applications of cathodoluminescence spectroscopy and imaging in the characterisation of pharmaceutical materials. European Journal of Pharmaceutical Sciences, 2012, 45(1−2): 19−42